High-depth-resolution 3-dimensional radar-imaging system based on a few-cycle W-band photonic millimeter-wave pulse generator

Tzu-Fang Tseng,[1] Jhih-Min Wun,[2] Wei Chen,[2] Sui-Wei Peng,[2] Jin-Wei Shi,[2,*] and Chi-Kuang Sun[1,3,4,5]

[1]*Department of Electrical Engineering and Graduate Institute of Photonics and Optoelectronics, National Taiwan University, Taipei, 10617, Taiwan*
[2]*Department of Electrical Engineering, National Central University, Taoyuan, 320, Taiwan*
[3]*Molecular Imaging Center and Graduate Institute of Bioelectronics and Bioinformatics, National Taiwan University, Taipei, 10617, Taiwan*
[4]*Research Center of Applied Science and Institute of Physics, Academia Sinica, Taipei, 11529, Taiwan*
[5]*sun@ntu.edu.tw*
[*]*jwshi@ee.ncu.edu.tw*

Abstract: We demonstrate that a near-single-cycle photonic millimeter-wave short-pulse generator at W-band is capable to provide high spatial resolution three-dimensional (3-D) radar imaging. A preliminary study indicates that 3-D radar images with a state-of-the-art ranging resolution of around 1.2 cm at the W-band can be achieved.

References and links

1. N. (Sami) Gopalsami and A. P. C. Raptis, "Millimeter-wave radar sensing of airborne chemicals," IEEE Trans. Microw. Theory Tech. **49**, 646–653 (2001).
2. J. K. Christensen and M. J. Underhill, "Phase coded pulse doppler and continuous wave 77GHz radar measurement and analysis facility," IEE Proc., Radar Sonar Navig. **151**(6), 365–374 (2004).
3. R. W. McMillan, C. W. Trussell, Jr., R. A. Bohlander, J. C. Butterworth, and R. E. Forsythe, "An experimental 225 GHz pulsed coherent radar," IEEE Trans. Microw. Theory Tech. **39**(3), 555–562 (1991).
4. Y.-W. Huang, T.-F. Tseng, C.-C. Kuo, Y.-J. Hwang, and C.-K. Sun, "Fiber-based swept-source terahertz radar," Opt. Lett. **35**(9), 1344–1346 (2010).
5. W. W. Camp, J. T. Mayhan, and R. M. O'Donnell, "Wideband radar for ballistic missile defense and range-doppler imaging of satellites," Lincoln Lab J. **12**, 267–280 (2000).
6. A. G. Stove, "Linear FMCW radar techniques," IEE Proc., Radar Sonar Navig. **139**, 343–350 (1993).
7. A. Y. Nashashibi, K. Sarabandi, P. Frantzis, R. D. De Roo, and F. T. Ulaby, "An ultrafast wide-band millimeter wave (MMW) polarimetric radar for remote sensing applications," IEEE Trans. Geosci. Rem. Sens. **40**(8), 1777–1786 (2002).
8. K. B. Cooper, R. J. Dengler, N. Llombart, T. Bryllert, G. Chattopadhyay, E. Schlecht, J. Gill, C. Lee, A. Skalare, I. Mehdi, and P. H. Siegel, "Penetrating 3-D imaging at 4- and 25-m range using a submillimeter-wave radar," IEEE Trans. Microw. Theory Tech. **56**(12), 2771–2778 (2008).
9. K. B. Cooper, R. J. Dengler, N. Llombart, A. Talukder, A. V. Panangadan, C. S. Peay, I. Mehdi, and P. H. Siegel, "Fast, high resolution terahertz radar imaging at 25 meters," Proc. SPIE **7671**, 76710Y, 76710Y-8 (2010).
10. N.-W. Chen, J.-W. Shi, H.-J. Tsai, J.-M. Wun, F.-M. Kuo, J. Hesler, T. W. Crowe, and J. E. Bowers, "Design and demonstration of ultra-fast W-band photonic transmitter-mixer and detectors for 25 Gbits/sec error-free wireless linking," Opt. Express **20**, 21223–21234 (2012).
11. J.-W. Shi, J.-W. Lin, C.-B. Huang, F.-M. Kuo, N.-W. Chen, C.-L. Pan, and J. E. Bowers, "Photonic generation of few-cycle millimeter-wave pulse using a waveguide based photonic transmitter mixer," IEEE Photon. J. **4**(4), 1071–1079 (2012).
12. M. A. Richards, J. A. Scheer, and W. A. Holm, *Principles of Modern Radar: Basic Principles* (SciTech publishing, 2010), Chap. 10.
13. D. R. Grischkowsky, "Optoelectronic characterization of transmission lines and waveguides by terahertz time-domain spectroscopy," IEEE J. Sel. Top. Quantum Electron. **6**(6), 1122–1135 (2000).
14. T.-A. Liu, G.-R. Lin, Y.-C. Chang, and C.-L. Pan, "Wireless audio and burst communication link with directly modulated THz photoconductive antenna," Opt. Express **13**(25), 10416–10423 (2005).

15. Z. D. Taylor, R. S. Singh, D. B. Bennett, P. Tewari, C. P. Kealey, N. Bajwa, M. O. Culjat, A. Stojadinovic, H. Lee, J.-P. Hubschman, E. R. Brown, and W. S. Grundfest, "THz medical imaging: In vivo hydration sensing," IEEE Trans. Terahertz Sci. Technol. **1**(1), 201–219 (2011).
16. H. Essen, M. Hagelen, A. Wahlen, K. Schulz, K. Jager, and M. Hebel, "ISAR imaging of helicopters using millimeter wave radars," Int. J. Microwave Wireless Technol. **1**(03), 171–178 (2009).
17. J.-W. Shi, F.-M. Kuo, and J. E. Bowers, "Design and analysis of ultra-high speed near-ballistic uni-traveling-carrier photodiodes under a 50 Ω load for high-power performance," IEEE Photon. Technol. Lett. **24**(7), 533–535 (2012).
18. J. Han and C. Nguyen, "A new ultra-wideband, ultra-short monocycle pulse generator with reduced ringing," IEEE Microw. Wirel. Compon. Lett. **12**(6), 206–208 (2002).
19. D. J. Benford, M. C. Gaidis, and J. W. Kooi, "Optical properties of Zitex in the infrared to submillimeter," Appl. Opt. **42**(25), 5118–5122 (2003).

1. Introduction

Millimeter wave (MMW) has been widely used in radar systems since it provides high penetration to a wide range of materials, as well as high reflection to dangerous metallic weapons and living objects with a high water content [1–4]. Compared with former radar systems operating in other bands with lower frequencies [5], a MMW radar system provides a higher spatial resolution with a reduced size of antenna. Generally there are three kinds of active radar systems: frequency-modulated continuous-wave (FMCW) radar system [6], chirp-pulse radar system [7], and short-pulse radar system [2,3]. Compared with FMCW (Fourier transform needed) and chirp-pulse radar system (pulse compression needed), short-pulse radar system has the potential of realizing real-time, extremely high-frame-rate (ex: 10 kHz or more), and high-spatial-resolution imaging without the need for complex signal processing in the receiver [2,3,6–9]. However, most of the reported MMW short-pulse radar systems had narrow bandwidths, and showed the radar imaging with the range resolution only on the order of meter or tens of meters [2,3]. To achieve a higher range resolution for far-distance sensing (> 20 meters), the sub-MMW radar system (~600 GHz) could provide a wide scanning bandwidth (~30 GHz) [8,9], and a range resolution as small as 1 cm has been successfully demonstrated. Nevertheless, compared with the other MMW bands in lower frequency regime, the free-space propagation loss at 600 GHz is much higher, which may limit the maximum sensing distance of such kind of high-resolution THz radar for military use [5]. As for the short distance application (< 4 meters) such as airport security examination, the lower operating frequency (~100GHz) can still reach the diffraction-limited image resolution of around 2 cm, which is sufficient for many threat scenarios [8].

In this paper we experimentally demonstrate that a near-single-cycle photonic millimeter-wave short-pulse generator is capable to provide three-dimensional (3-D) MMW radar imaging with a 1.2cm range resolution in W-band, which is an important MMW window for high data rate wireless communication [10] and environmental monitoring [1,3,4]. The MMW radar system is driven by the near-single-cycle photonic millimeter-wave short-pulse generator [11] at the W band. By use of such a radar system, a metallic object with 3-D profile has been measured and its 3-D imaging has been reconstructed successfully to verify the high longitudinal resolution of the proposed technique. In this work, the detail about the photonic pulse generator and our algorithm for imaging acquisitions has been well discussed.

In our pulse generator, the short electrical transient is photonically generated in the MMW WR-10 waveguide [11] and the generated pulse signal can be directly amplified or processed through the use of commercial available waveguide-based active/passive MMW components. Usually, in order to further improve the maximum sensing distance of the proposed short-pulse radar system, a traveling-wave tube or magnetron-based oscillator with a very-high peak saturation power (under pulse-mode operation) is necessary [12]. For such a case, our photonic scheme possesses the unique advantage of excellent isolation between the input local oscillator (LO: sinusoidal MMW signal in optical domain) and output millimeter wave signals while maintaining a short pulse-width. In addition, as compared to the optical rectification or the photo-Dember effect that are commonly employed methods in obtaining sub-ps electrical pulses in free-space [13–15], our waveguide based approach provides a

much higher output power and less distortion in the generated waveform [11]. As a result, the acquisition of 3-D radar image becomes feasible.

With a 3-dB bandwidth of around 12GHz, the range resolution of our radar system is around 1.2 cm (4 times of the wavelength), without the need for complex signal processing in the receiver. The sensing distance is around 1.2 meter and can reach longer to 2-4 meters. Comparing to other previous MMW radar systems (FMCW and chirp-pulse radar systems included) [2,3,7,16] with a traditional electronic approach, the demonstrated range resolution is much higher due to the short pulse-width. As a result with further improvement, our short-distance radar system is with a high potential to provide real time imaging with an ultra-high frame rate.

2. Pulse generation scheme

The schematic diagram of the photonic generated W-band short pulse radar system is shown in Fig. 1(a). Our near-ballistic uni-traveling carrier photodiode (NBUTC-PD) [17] based photonic transmitter-mixer (PTM) at W-band, which has a wide intermediate frequency (IF) modulation bandwidth (~25 GHz) [10] and an ultra-wide optical-to-electrical (O-E) bandwidth (~250 GHz) [17], was previously designed to convert the optical excitation envelope to MMW signals for photonic wireless communication [10]. In this study, the NBUTC-PD was flip-chip bonded onto an aluminum nitride (AlN) substrate with a high thermal conductivity with a slot-line metallic pattern, as shown in Fig. 1(b), for high-power MMW generation and switching [10,17]. In this setup, the 94 GHz MMW carrier frequency was simply generated by the use of two-laser heterodyne beating technique. A conceptual diagram of the beating waveform (94 GHz optical LO) is also shown in Fig. 1(a). Where, the envelope represents the 94 GHz sinusoidal signal and the carrier wave inside represents the frequency of the optical signal at around 1.55 μm wavelength. The PTM was under a reverse DC bias voltage at around 1 to 2V, for optimum dynamic performance, which will be discussed later. To generate a short-pulse waveform, a 46ps electrical pulse train with around 1V peak-to-peak voltage swing from an electrical pulse pattern generator (PPG) (Anritsu MP 1800A) was directly fed onto our device through a V-band on-wafer probe, to swing the bias voltage of the PTM. Due to strong nonlinearity of the active NBUTC-PD under bias modulation, the injected electrical pulse train would be mixed with the photo-generated MMW LO signal and then up-converted to the W-band (94 GHz) frequency regime. During the experiment, these up-converted MMW pulses were picked up by another on-wafer W-band MMW probe on the other side of device. The pulse repetition rate generated from the PPG has the frequency range between 100 MHz and 12.5 GHz, and was set to be 1.25 GHz (800 ps repetition time) in our radar system. To provide high radiated peak power for a long sensing distance, an additional W-band power amplifier (QuinStar, QPW-78A51620-P2) was necessary in our scheme to amplify the up-converted electrical pulse. Its maximum P_{1dB} output saturation power is around + 16 dBm. In the receiving end, a receiving horn antenna (receiving HA) was used with an ultrafast W-band envelope detector (Virginia Diode, WR 10R3 1-14), to detect the envelope of the received pulse. A W-band low noise amplifier (LNA) (Millitech, LNA-10-02150) was connected to the sampling scope to measure and retrieve the received waveform with a higher signal-to-noise ratio. The trigger of the sampling scope was provided by the internal clock of PPG.
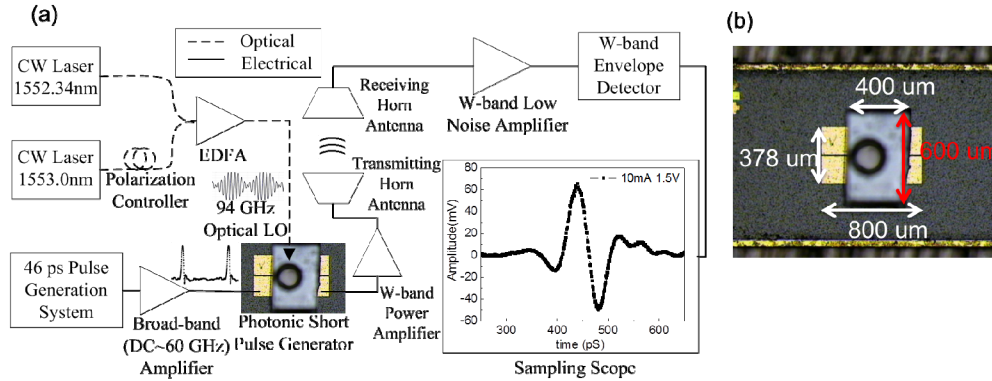
Fig. 1. (a) The schematic diagram of the near-single-cycle W-band MMW pulse measurement. (b) The photo of NTUTC-PD.

In order to investigate the intrinsic performance of our photonic pulse generator, at first, we have removed the W-band power amplifier and transmitting/receiving horn antenna in our system and performed the impulse response measurement. For such measurement, our receiver (W-band LNA and envelope detector) was directly connected with our W-band on-wafer probe to capture the envelope of up-converted MMW pulse. Figure 2(a) shows the measured envelope of impulse responses under a fixed output photocurrent at ~14 mA and different reverse bias voltages. By increasing the reverse bias voltage from 0.8 to 1.8 V, we can find that the pulse-width significantly shortened from 77 to 54 ps. Figure 2(b) shows in detail the variation of the full-width half maximum (FWHM) of measured pulse-envelope versus reverse bias voltage under different output photocurrents. As can be seen, by boosting up the operation photo-current, the measured pulse-width can be reduced significantly, which accompanies the increase in required optimum reverse bias voltage. The observed improvement in modulation speed with the increase of photocurrent can be attributed to the bandwidth enhancement effect of NBUTC-PD under high-power operation [10,17]. However, as shown in Fig. 2(c), such an increase in reverse bias voltage would lead to the reduction in the output peak amplitude. This phenomenon can be explained by the nonlinear transfer curve of NBUTC-PD. Figure 3 shows the generated MMW power of our NBUTC-PD under a 15 mA output photocurrent versus reverse bias voltages. As shown in Fig. 3, in order to generate the highest MMW power variation (amplitude) under a 15 mA output photocurrent, the optimum reverse DC operation point should be around 1.1 V with a 1 V peak-to-peak AC driving voltage. In addition, further increase in the reverse DC bias point (> 1.1 V) during bias modulation would definitely reduce the peak amplitude and shorten the width of the generated pulses.
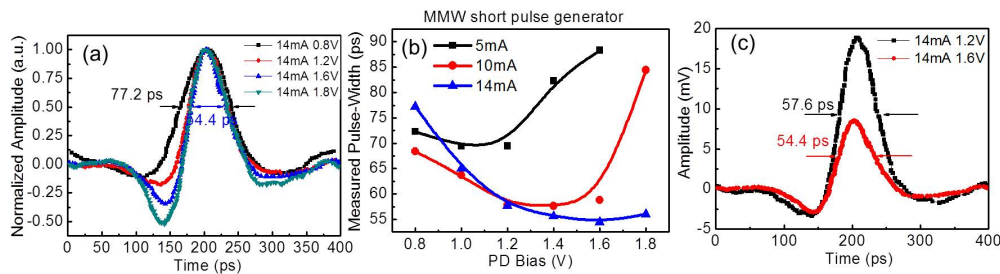

Fig. 2. (a) The measured pulse-width versus the bias voltage on PD. (b) The measured pulse width versus PD bias voltage at different photocurrent. (c) The measured pulse amplitude at different PD bias voltages.
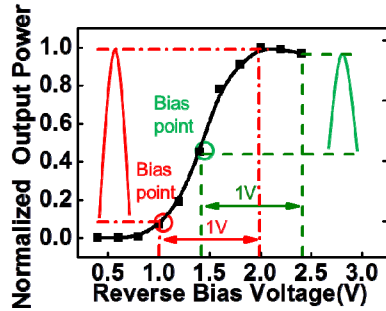
Fig. 3. The generated MMW power and output photocurrent of our NBUTC-PD versus reverse bias voltages

In order to determine the optimized operation condition for our short-pulse radar imaging experiment, we then measured the impulse responses under different output photocurrents and bias voltages by connecting our photonic pulse generator with the W-band power amplifier and transmitting horn antenna. During such measurement, the receiving horn antenna was set 10 cm away from the transmitting antenna, without any objects in between. Figures 4(a)–4(c) show the measured envelope waveforms after normalization, their full-width half maximum (FWHM) versus reverse bias voltages under different output photocurrents, and the measured envelope waveform without normalization, respectively. As can be seen, these traces exhibit similar trend with what we discuss in Figs. 2. A significant trade-off between pulse-width and amplitude can be observed. During our radar imaging experiment, in order to get a short pulse-width with reasonable high peak amplitude, we chose the operation photocurrent and reverse bias voltage at 10 mA and around 1.6 V, respectively. The corresponding waveform is shown in Fig. 1(a). Furthermore, after integrating with the W-band power amplifier during pulse measurement and comparing the waveform with the measured traces shown in Figs. 2, we can clearly see the negative tail which would sharpen the measured positive impulse response. The formation of the negative tail can be attributed to the uneven frequency response of W-band power amplifier. Figure 5(a) shows the frequency response of the W-band power amplifier. As can be seen, for our case with the 94 GHz operating central frequency as reference, there exists a ~4 dB enhancement in magnitude at 84 GHz. Figure 5(b) shows the measured impulse response (black trace) and the same waveform after truncating the ringing tail (red trace). Figure 5(c) shows the corresponding fast-Fourier-transformed (FFT) frequency responses of these two waveforms. The transformed spectrum in Fig. 5(c) clearly indicates that there was a significant resonant frequency at ~10 GHz, which corresponds to the separation of central operating frequency (94 GHz) and peaking frequency (84 GHz) of our power amplifier. In addition, the ripple in the FFT spectrum (black trace in Fig. 5(c)) is mainly originated from the ringing tail of impulse response (black trace in Fig. 5(b)). By truncating such ringing tail (red trace in Fig. 5(b)) during FFT process, the transformed spectrum would become smooth, as the red trace shown in Fig. 5(c). Such a low frequency ringing tail would degrade the range resolution of the radar system, and can be eliminated by using the high-pass filter (pulse shapers) integrated with the receiver end [18] or using some signal processing techniques, which will be discussed latter.
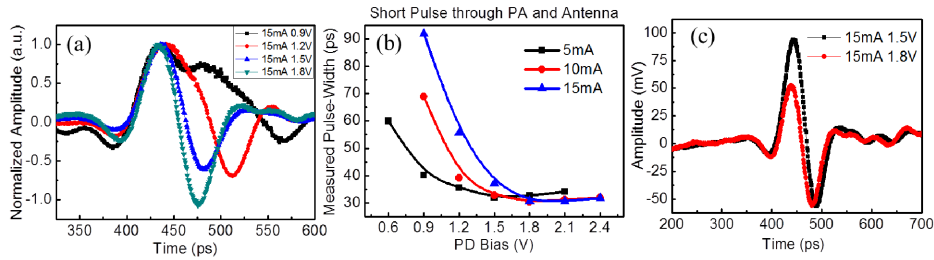
Fig. 4. (a) The measured pulse-width versus bias voltage on PD. (b) The measured pulse width versus PD bias voltage at different photocurrent. (c) The measured pulse amplitude at different PD bias voltages.
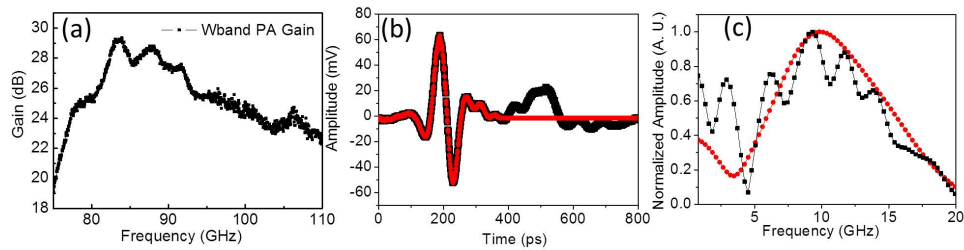

Fig. 5. (a) The measured frequency response of the W-band power amplifier. (b) The measured impulse responses without (black trace) and with (red trace) truncating ringing tail. (c) The corresponding FFT spectra of the two waveforms in (b).

3. W-band short pulse radar system setup and measurement

The short pulse radar system setup is shown in Fig. 6. In order to achieve a relative high transverse range resolution, a MMW bulk lens with a 60 cm diameter (Millitech) was put around 60 cm behind the transmitting horn antenna. The incident wave from the horn antenna passed through the lens and focused around 60 cm behind the lens, where the object under test (OUT) was installed. In order to investigate the waveform and spot size of the incident pulse onto OUT during measurement, the receiver, which is shown as part (B) in Fig. 6, was first put at the focal plane of the MMW lens (as shown in part (A) in Fig. 6). The measured spot size, waveform, and Fourier transform of the waveform, are shown in Figs. 7(a)–7(c) respectively. The waveform had a 70 mV peak-amplitude, and its 3-dB bandwidth was around 13 GHz, which is almost the same as the bandwidth of the pulse without passing the MMW lens, as shown in Fig. 5(b). As shown in Fig. 6, our OUT was a pattern of angry-bird with different heights among different points, and had a metallic surface which is opaque under the MMW illumination. For imaging experiment the receiver was installed on the same side with the transmitting horn antenna to capture the reflected waveforms from the OUT. By using the sampling scope to determine the time difference between the reflected waveforms from the OUT, we can thus construct the surface profile of OUT in the longitudinal direction. In order to obtain the a 3-D image for a resolution study, the OUT was put on the 2-D translation stage (Zaber Technology, A-LSQ150D-E01) and was raster-scanned with one pixel area of 1 cm x 1 cm.
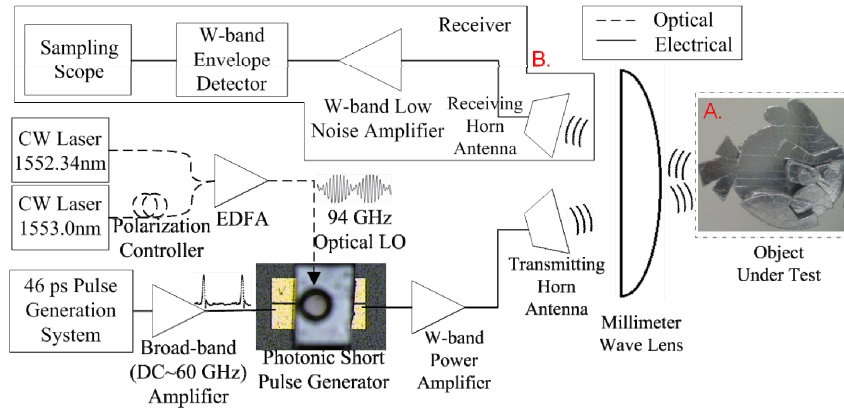
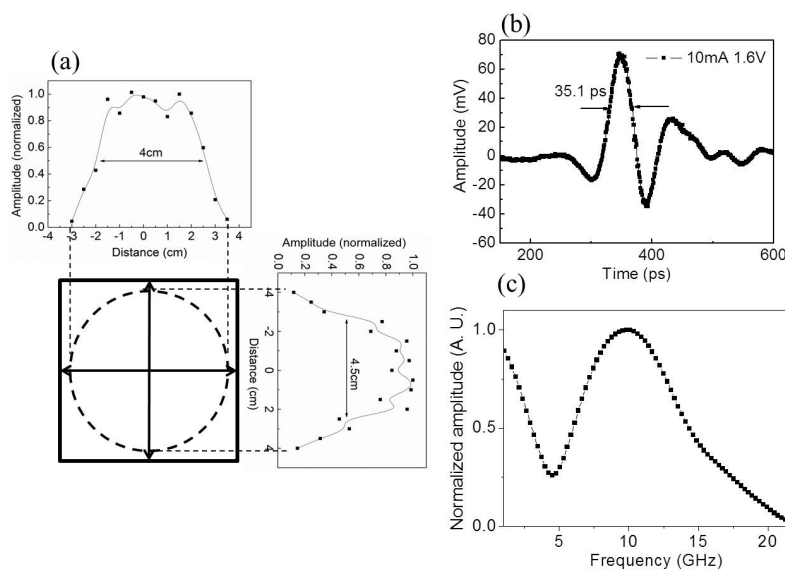Fig. 6. The schematic diagram of the near-single-cycle W-band MMW pulse radar system.

Fig. 7. (a) The measured spot size at the focus of the MMW lens. (b) The measured waveform of the short pulse at the focus of the MMW lens. (c) The Fourier transform of the waveform.

Figures 8(a)–8(b) show a typical reflected waveform captured by our receiver (Part B in Fig. 6) and its corresponding Fourier transformed frequency response, respectively. As can be seen, due to the double-pass through the MMW lens, a slight broadening of the pulse-width and a decrease in the transformed bandwidth has been observed. According to the frequency response in Fig. 8(b), our 3 dB system bandwidth is around 12 GHz. The corresponding range resolution, which can be calculated as c/(2xBW), of our whole imaging system in the longitudinal direction (the direction of pulse propagation) was at around 1.2 cm. c is the light speed and BW is the 3 dB bandwidth of the transformed frequency response. The signal to noise ratio (SNR) of every pixel was around 18 dB calculated from the reflected waveform. Such a value of SNR was limited by the insertion (dielectric) loss of the Teflon made MMW lens [19], which can be minimized by further reducing the size and thickness of such a bulky MMW lens.

Regarding the transverse resolution, it is limited by the spot size (~4.5 cm in diameter) of our MMW beam, which is shown in Fig. 7(a). In order to further improve the resolution, we have developed a signal processing algorithm for image acquisition, which will be discussed latter.
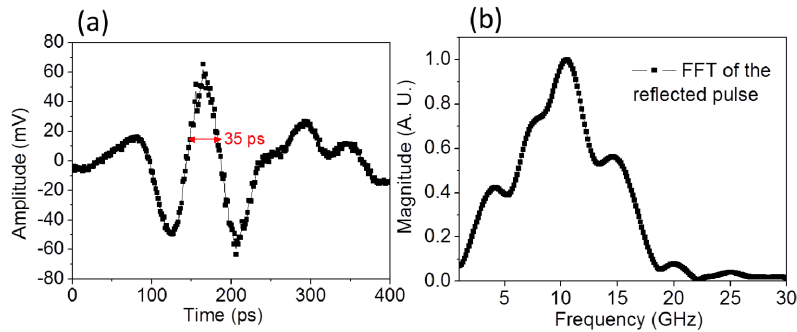
Fig. 8. (a) One example of the reflected waveform from a flat metallic surface. (b) The Fourier transform of the waveform.

4. Results and discussion

In order to further improve the transverse resolution, the oversampling technique has been adopted, which means that during the reconstruction process of the 3-D profile of a single pixel, we must simultaneously analyze the measured waveforms of its surrounding pixels. During each single pixel measurement, we may expect that there are several reflected pulses in the measured trace, which represents the change in depth of surface profile. This is because that our large MMW spot size (4.5 cm in diameter) would cover the complex surface profile with different depths existed in a single pixel. By comparing the measured waveforms with those of its surrounding pixels, we can thus accurately map the reflected pulses in different time slots to the different transverse locations. Figures 9(a)–9(b) show the examples of such imagine acquisition process (oversampling). In order to precisely construct the profile of pixel (M) with enhanced resolution, nine pixels (M, U, L, R, D, UL, UR, DL, and DR) were measured on the OUT at the same time and their corresponding reflected waveforms were given in Figs. 9(a) and 9(b), respectively. The earlier and latter pulses in the time scale of these traces represent a shallower and deeper profile of every pixel in the longitudinal direction, respectively. The ringing tail behind the main pulse has been eliminated directly by setting an optimized threshold value during signal processing, which would smooth the frequency response of FFT spectrum (as discussed in Fig. 5) and greatly enhance the quality of imaging as discussed latter. Since the ringing tail usually has the peak amplitude less than one-third of that of the main pulse, we thus chose the threshold value as the one-third of the peak amplitude of main pulse in each measured waveform.

For the measured waveforms with a single peak, such as the traces of pixels UR, R, L, and D, the pixels were considered to locate at the places without change in depth. While for the traces of pixels such as DL and M, there were two (or more) peaks in the measured waveforms, which revealed a change in the depth inside these two pixels. We divided nine small grids in a single pixel, as shown in Fig. 9(a), and arranged the time of the different peaks at proper grids, by comparing with the time of the measured peaks of its eight neighboring pixels. Take pixel M for example, at first, we arranged the reflecting time of the highest peak (red open circle in Fig. 9(b)) in nine grids. Then, the time of the second peak was then compared to that of the waveforms of its neighboring pixels (U, L, R, D, UL, UR, DL, and DR). We can clearly see that the peaks of its surrounding pixels UR and R occur at the same temporal positions as that of the second peak on M, as shown in Fig. 9(b). We thus assigned the height of the upper-right and right corner grids according to the second temporal peak as marked in red solid circle, which represents the reflecting time of the second peak. In Fig. 9(b), the reflecting time of the first peak was marked as open circle.
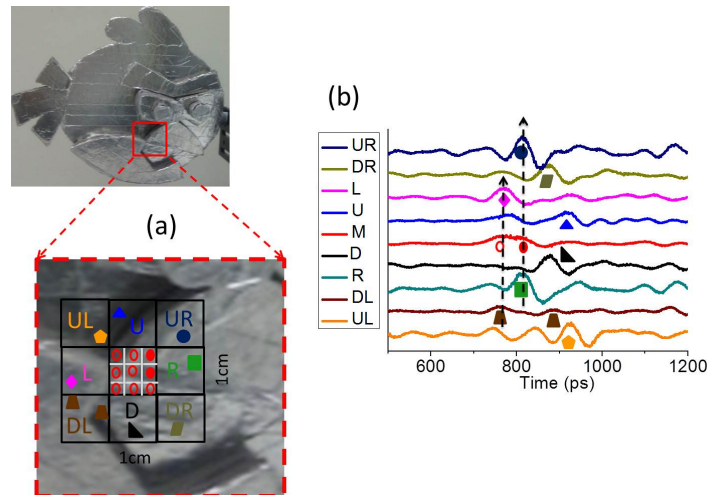
Fig. 9. (a) The photo of OUT which shows the different depths of every pixel. (b) The captured waveforms correspond to the depths of the nine pixels.

Figures 10(a)–10(c) show the photo of OUT and the reconstructed 3-D image with 12 x 12 pixels. As can be seen, the reconstructed image is close to but doesn't completely match the actual profile of the OUT. Take pixel M for example, there are total four different depths in such pixel. However, only two peaks were picked out, and the MMW-resolved depth profile would thus differ from the real one. In order to get further improvements in system resolution, it is necessary to further reduce our transverse spot size by using more advanced quasi-optics setup and boosting up the operating central frequency [8]. In addition, the elimination of ringing tail by setting an optimized threshold value also plays an important role in the quality of reconstructed imaging. Without any threshold setting, the reconstructed image would be failed and unrecognizable, as shown in Fig. 10(d).

To verify our high depth resolution, the actual and measured depths at several positions (pixels) were compared, and the results are shown in Table 1. As can be seen, the measured errors are usually less than 5% (< 0.2 cm). This result confirms that our proposed photonic MMW short-pulse radar can really offer a depth resolution as high as ~1.2 cm. Table 2 shows the comparisons between our system, and the reported MMW radar systems with short pulse, chirp pulse, and FMCW techniques. Our 3-D short-pulse radar imaging system shows the state-of-the-art range resolution of around 1.2 cm in W-band. Our achieved range resolution is even comparable with that of a reported FMCW radar system operated at a much higher central frequency (100 vs. 600 GHz) [8,9] with a much higher free-space propagation loss. The maximum sensing distance (~1.2 meter) in our proposed system is limited by the focus length (f) of the adopted MMW lens. A longer sensing distance (2-4 meters) can be expected by further improving our quasi-optical antenna system [8,9]. Where, several lens antennas for collimating and focusing the MMW beam is necessary.
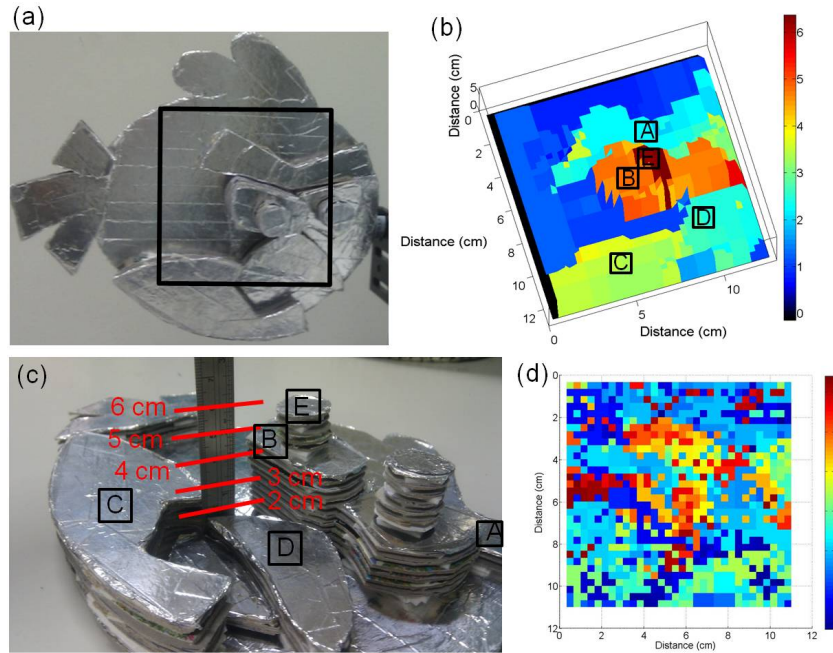
Fig. 10. (a) The scanning area of the angry-bird pattern. (b) The reconstructed 3-D image. The color bar shows the height with the unit of centimeter (cm). (c) The profile of the angry-bird pattern. (d) The failed image reconstruction without threshold setting.

Table 1. Comparisons of the actual and measured depth of the object

Position	A	B	C	D	E
Actual depth (cm)	1.2	3.6	2.3	1.7	5.4
Measured depth (cm)	1.4	3.6	2.4	1.6	5.3
Error (%)	17%	0%	4%	6%	2%

Table 2. Comparisons of Different MMW Radar Systems

MMW Radar System	Central Frequency	Type (short pulse / chirp pulse / FMCW)	Bandwidth	Range Resolution	Sensing Distance
Ref [2]	77 GHz	Short pulse	75 MHz	200 cm	> 500 cm
Ref [3]	225 GHz	Short pulse	2 –20 MHz	> 750 cm	3750-350000 cm
Ref [7]	95 GHz	Chirp pulse	840 MHz	> 20 cm	1000-5000 cm
Ref [16]	94 GHz	FMCW	800MHz	19 cm	20000 cm
Ref [8]	590 GHz	FMCW	30GHz	0.5-1cm	<2500 cm
*Our System	94 GHz	Short pulse	~12 GHz (3dB)	~1.2 cm	120 cm

5. Conclusion

In conclusion, we have demonstrated that a near-single-cycle photonic millimeter-wave short-pulse generator at W-band is capable to provide high spatial resolution for future 3-D radar imaging. A raster scanning system shows that 3-D imaging with a longitudinal range resolution of 1.2 cm can be obtained in W-band. With further improvement, this short-

distance radar imaging system is with a strong potential to provide real-time imaging with an ultra-high frame rate.

Acknowledgment